Nanoscale

AgPd Nanoparticles for the Electrocatalytic CO2 Reduction: Bimetallic Composition-Dependent Ligand and Ensemble Effects

Journal:	*Nanoscale*
Manuscript ID	NR-ART-04-2020-003203.R1
Article Type:	Paper
Date Submitted by the Author:	30-May-2020

Complete List of Authors:	Cui, Meiyang; University of Virginia, Chemistry Johnson, Grayson; University of Virginia, Chemistry Zhang, Zhiyong; University of Virginia, Department of Chemistry Li, Shuang; Brookhaven National Laboratory Hwang, Sooyeon; Brookhaven National Laboratory, Center for Functional Nanomaterials Zhang, Xu; California State University Northridge, Physics and Astronomy Zhang, Sen; University of Virginia, Chemistry

Nanoscale

AgPd Nanoparticles for the Electrocatalytic CO_2 Reduction: Bimetallic Composition-Dependent Ligand and Ensemble Effects

Received 00th January 20xx,
Accepted 00th January 20xx

DOI: 10.1039/x0xx00000x

Meiyang Cui,[a] Grayson Johnson,[a] Zhiyong Zhang,[a] Shuang Li,[b] Sooyeon Hwang,[b] Xu Zhang,[c] and Sen Zhang*[, a]

Monodisperse AgPd nanoparticles (NPs) were synthesized and studied as an efficient catalyst for electrocatalytic CO_2 reduction by modulating bimetallic compositions. The mechanistic studies, based on density functional theory (DFT) calculations and environmental diffuse reflectance infrared Fourier-transform spectroscopy (DRIFTS) analysis, revealed that the incorporation of Ag in AgPd NPs can effectively weaken CO adsorption on all possible Pd surface sites (the ligand effects), and more importantly, disrupt the strongest multi-centered CO-binding sites (the ensemble effects). With properly tuned CO adsorption, which is ordinarily too strong over pure Pd, $Ag_{15}Pd_{85}$ NPs were found to be the best composition for the efficient production of CO. It delivers a unity conversion of CO_2 to CO with a high mass activity of 15.2 mA mg_{metal}^{-1} at -0.8 V vs. reversible hydrogen electrode (RHE) and a high stability with minimal change in the CO Faradaic efficiency (FE_{CO}) after 12 hours of operation.

1

Introduction

Electrocatalytic CO_2 reduction reaction (eCO_2RR) offers the possibility of carbon-neutral production of chemicals and fuels when driven by renewable electricity (solar, wind and hydro etc.).[1-3] CO is one of the targeted eCO_2RR products with broad interest, as it is an essential precursor in many industrial processes, including the water-gas shift reaction for hydrogen production as well as the chemical synthesis of methanol, acetic acid, and aldehydes etc.[1, 4] Thermodynamically, the eCO_2RR to CO takes place at -0.52 V vs. standard hydrogen electrode (SHE).[5, 6] However, due to the sluggish kinetics and multi-step proton and electron transfers, the reaction usually requires large overpotentials to yield a desirable production rate of CO.[7,8]

Among the various metal catalysts studied for the eCO_2RR, Pd has shown an impressive Faradaic efficiency towards CO (FE_{CO}) at relatively low overpotentials.[9] This is primarily caused by the strong binding energy of C-bound intermediates (including *CO, *COOH etc. that are correlated through a scaling relationship) in the surface of Pd, facilitating CO_2 activation and suppressing the competing hydrogen evolution reaction (HER)[10, 11]. But this feature makes Pd prone to CO-poisoning,[12] which hampers the CO desorption step and decreases the CO production rate.[13] A great deal of effort is devoted to balancing the binding energy of C-bound intermediates for improved efficiency by tuning the size and surface structure of Pd nanoparticles (NPs). For example, Gao et. al. investigated the size effect of Pd NPs (from 2.4 to 10.3 nm) and demonstrated that a 91.2% FE_{CO} can be reached on 3.7 nm Pd.[14] Pd concave nanocubes with high index {310} surface facets were found to be more efficient than Pd nano-octahedrons and nanocubes, leading to a FE_{CO} of 90.6%.[15] Despite the encouraging progress, the issue of low CO current density (production rate) associated with over-strong CO adsorption over Pd NPs needs to be further addressed.

Alloying Pd with a second element, M, has been studied to lower the CO adsorption strength and enhance the CO production rate. Yin et. al. reported that CuPd alloy NPs can exhibit a significantly improved CO mass current density.[16] Yet the FE_{CO} dropped down to 86% because of the promoted HER at the Cu sites. Such a M-induced product selectivity alteration was also observed on other MPd alloy NPs (such as NiPd,[17] SnPd[18] etc.). In this article, we specifically studied AgPd NPs with a uniform size of 2-4 nm and controllable AgPd bimetallic compositions to elucidate the composition-dependent catalytic property for the eCO_2RR. Ag is a known metal with weak binding to both *CO and *H.[10] We anticipate the incorporation of Ag into Pd can alleviate CO-poisoning without sacrificing the FE_{CO}. A similar concept was employed to construct Pd small clusters in the surface of Au NPs,[19] but the use of Ag in the present work

[a] Department of Chemistry, University of Virginia, Charlottesville, VA 22904, United States.
[b] Center for Functional Nanomaterials, Brookhaven National Laboratory, Upton, New York 11973, United States.
[c] Department of Physics and Astronomy, California State University Northridge, Northridge, California 91330, United States.
* Corresponding author. E-mail: sz3t@virginia.edu
Electronic Supplementary Information (ESI) available: [details of any supplementary information available should be included here]. See DOI: 10.1039/x0xx00000x

benefits from the ease of synthesizing atomically precise AgPd NPs as well as the higher efficiency and earth abundance of Ag. By systematically studying AgPd NPs with a wide range of well-controlled compositions, $Ag_{15}Pd_{85}$ is identified as the most efficient with a FE_{co} at 100% and a high CO current density of 15.2 mA mg_{metal}^{-1} at -0.8 V vs. reversible hydrogen electrode (RHE). With the assistance of density functional theory (DFT) calculations and environmental diffuse reflectance infrared Fourier-transform spectroscopy (DRIFTS) analysis, we further demonstrate that the bimetallic enhancement arises from a combination of ligand and ensemble effects that is properly adjusted by the favourable Ag level. The former weakens the CO adsorption on all possible Pd sites, while the latter disrupts the strongest multi-fold CO binding sites.

Experimental

Chemicals and Materials

Palladium(II) acetylacetonate ($Pd(acac)_2$, >99%), Silver(I) acetate (Ag(ac), 99%), oleic acid (OAc, 90%), olyelamine (OAm, 70%), Nafion (5 wt% in lower aliphatic alcohols and water) were purchased from Sigma-Aldrich. 1-Octadecene (ODE, 90%) was purchased from Acros Organics. Hydrazine monohydrate (>99%) was purchased from Alfa Aesar. Isopropanol (99.5%) and hexanes (98.5%) were purchased from Fisher Scientific. Vulcan-XC 72R carbon black was obtained from Fuel Cell Store. All chemicals and materials were used as received without further purification.

Synthesis of AgPd, Ag, and Pd NPs

All AgPd NPs with different bimetallic compositions were synthesized via an organic-phase colloidal approach, according to our previous report.[20] In a typical synthesis of $Ag_{15}Pd_{85}$ NPs, 244 mg of $Pd(acac)_2$ (0.8 mmol) and 34 mg of Ag(ac) (0.2 mmol) were mixed together with 4.5 ml of OAc, 0.5 ml of OAm, and 10 ml of ODE. The mixture was kept at 60 °C under N_2 atmosphere for 30 minutes to generate a transparent, dark orange solution. It was heated to 180 °C at a ramp rate of 3-5 °C min^{-1} and was then kept at that temperature for 20 minutes. After cooling down to the room temperature, the NPs were collected by centrifugation at 8000 rpm after the addition of 45 ml of isopropanol. Then, the NPs were purified twice by centrifugation in 5 ml of hexane and 40 ml of isopropanol. The as-synthesized NPs were re-dispersed and stored in hexanes. Following the same procedure, Ag_5Pd_{95}, $Ag_{37}Pd_{63}$ and $Ag_{45}Pd_{55}$ NPs were synthesized by using 274 mg (0.9 mmol) of $Pd(acac)_2$ together with 16.7 mg (0.1mmol) of Ag(ac), 183 mg (0.6 mmol) of $Pd(acac)_2$ together with 67 mg (0.4 mmol) of Ag(ac), and 152 mg (0.5 mmol) of $Pd(acac)_2$ together with 84 mg (0.5 mmol) of Ag(ac), respectively.

For the control experiment, Ag NPs were prepared with 167 mg of Ag(ac) as the sole metal precursor following the same synthetic strategy of AgPd. We also obtained Pd NPs with the similar size according to an established method.[21] 100 mg of $Pd(acac)_2$ was dissolved in 12 ml of OAm under magnetic stirring. After degassing the solution at 60 °C for 30 minutes to remove the moisture and impurities, 200 mg of TBAB that was pre-dissolved in 3 ml of OAm was injected into the reaction system. The solution was kept for 30 minutes before cooling to room temperature. The Pd NPs were collected and purified following the same procedure of AgPd NPs as detailed above.

Preparation of Carbon Supported NPs (C-NPs) Catalysts

200 mg of carbon black (Vulcan XC 72R) was dispersed in 10 ml of hexanes under sonication for 15 min. 50 mg of the as-prepared NPs (dispersed in hexanes) was then added dropwise into the carbon black suspension and sonicated for 1 hour. The supported NPs were then collected by centrifugation, washed with ethanol, and dried in a vacuum oven overnight. To remove OAc and OAm surfactants attached to the NPs surface, the catalyst was stirred in 10% v/v hydrazine/ethanol solution overnight, and then washed three times by centrifugation (5000 rpm, 5 minutes) with the addition of 20 ml of ethanol. The catalyst was dried under vacuum before its use.

Characterizations

Transmission electron microscopy (TEM) images were obtained on a FEI Tecnai Spirit (120 kV). High resolution TEM (HRTEM) images were obtained on a FEI Titan 80-300 (300 kV). Scanning TEM (STEM) analyses were carried out using a Hitachi HD2700C (200 kV) equipped with a probe aberration-corrector and an electron energy loss spectroscopy (EELS) detector in the Center for Functional Nanomaterials at Brookhaven National Laboratory. The 2D EELS elemental mappings were collected using a high resolution Gatan-Enfina ER with a probe size of 1.3 Å. A power law function was used for EELS background subtraction. Inductively coupled plasma optical emission spectrometry (ICP-OES) analyses were conducted on a PerkinElmer Avio-200 ICP Optical Emission Spectrometer to determine the compositions of AgPd NPs and the metal loading on the C-NPs catalysts. X-ray diffraction (XRD) characterizations were carried out on an Empyrean Multipurpose X-Ray Diffractometer with Cu Kα radiation (λ = 1.5418 Å). X-ray photoelectron spectroscopy (XPS) was carried out using a PHI VersaProb III which is equipped with a monochromatic Al k-alpha X-rays (1486.6 eV) to identify the surface composition and electronic structure of the catalysts. Diffuse reflectance infrared Fourier-transform spectroscopy (DRIFTS) was carried out to measure the adsorbed CO profiles using a Nicolet iS 50 FT-IR (Thermo Scientific, USA) equipped with a DiffusIR™ diffuse reflectance cell (Pike Technologies). After the sample was loaded into cell, it was first purged with Ar (50 sccm) at room temperature for 1 hour, and the background was collected. Then CO (1% balanced in Ar) was introduced into the chamber and purged (25 sccm) for another 1 hour until the sample was completely saturated. The CO desorption behavior was studied by flushing the sample with Ar (25 sccm) again at designed temperature 303 K, 353 K, 403 K and 453 K. The ramping rate is 5 °C min^{-1}.

Electrocatalytic Analysis

The eCO_2RR was investigated in 0.1 M $KHCO_3$ electrolyte solution, using an Autolab Potentiostat (PGSTAT128N, Metrohm AG, Switzerland), a glassy carbon working electrode (5 mm in diameter), a Ag/AgCl electrode reference electrode, and a Pt gauze counter electrode. All potentials were reported vs. reversible hydrogen electrode (RHE) using the following the equation:

$$E(\text{vs. RHE}) = E(\text{vs. Ag/AgCl}) + 0.197 + 0.0591 \times \text{pH} \quad (1)$$

To prepare the working electrode, 2 mg of the catalyst (~20 wt%) was first sonicated in 200 µl isopropanol and 5.1 µl of Nafion (5 wt%) for 1 hour to form a uniform ink. An appropriate amount of the ink was then dropcast onto a pre-polished glassy carbon electrode to yield a loading of 250 µg of carbon

supported catalysts. The real metal loading on the electrode was subsequently calculated based on this number and the metal concentrations determined by ICP-OES analysis (Table S1). The electrocatalysis was performed in a gas-tight H-type cell with a Nafion-212 membrane assembled between the cathode and anode compartments. Each chamber was filled with 12 ml of 0.1 M $KHCO_3$ electrolyte. Cyclic voltammetry (CV) measurements were performed in a CO_2-saturated 0.1 M $KHCO_3$ electrolyte at 20 mV s^{-1}. To assess the product distribution, controlled potential electrolyses (CPE) were performed at selected potentials. During the electrolysis, CO_2 was steadily supplied to the cathode compartment at a rate of 10 sccm, and the gas phase effluent in the headspace of the cathode compartment was continuously introduced to the sampling loop of a Shimadzu gas chromatograph (GC2014). The gaseous product stream was analysed by a thermal conductivity detector (TCD) and a flame ionization detector (FID) equipped with a methanizer, using argon as the carrier gas. The liquid phase products were analysed using a Shimadzu high-performance liquid chromatography (HPLC) equipped with a Bio-rad Aminex HPX-87H column, a photodiode array detector (PDA), and a reflective index detector (RID), using a 5 mM H_2SO_4 mobile phase.

DFT Calculations

Density functional theory (DFT) calculations were performed using the Vienna ab initio simulation package (VASP)[22] with the projector augmented wave (PAW) pseudopotentials[23] and the revised Perdew-Burke-Ernzerhof (RPBE) exchange correlation functional.[24] An energy cutoff of 450 eV was used for the plane wave basis set. The energy convergence criterion was 10^{-6} eV for geometry optimizations.

All adsorption energy calculations were performed on the (111) surface of the Ag, Pd, and AgPd alloy systems. The surface was modelled by a (1x2) supercell comprised of 4 layers and 15 Å of vacuum. The bottom layer was frozen to the bulk parameter while the top 3 layers were allowed to fully relax. A 3 x 3 x 1 Monkhorst – Pack k – point mesh[25] was the chosen sampling scheme. The binding energy between CO and the surface was sampled at atop, bridge, *hcp* three-fold hollow, and *fcc* three-fold hollow sites on the pure metals and alloys and is given by the equation.

$$E_{b,CO} = E(CO + slab) - E(Slab) - E(CO) \quad (2)$$

The CO coverage is held at $\theta = 1/16$. The Ag concentration was varied from 0 to 100% in 12.5% (to 25%) and then 25% intervals. Lattice parameters for each pure metal and the alloys were calculated to be 3.98 Å, 4.04 Å, 4.10 Å, 4.14 Å, and 4.22 Å from Pd to Ag, comparing favorably with previous work after accounting for the slight increase expected with the use of the RPBE functional.[24, 26]. Since the Pd three-fold hollow sites do not exist in the $Ag_{50}Pd_{50}$ and $Ag_{75}Pd_{25}$ (111) slab model surfaces, we generate the three-fold Pd ensembles by rearranging the surface atoms but keeping the chemical composition fixed on the surface (see Fig. 5a-d, Fig. S12 for models). These generated structures were fully relaxed and served as the reference for the relevant binding energy calculations.

Results and Discussion

The AgPd NPs were prepared via a colloidal synthetic approach that we reported previously,[20] using OAm as the reducing agent and the combination of OAc and OAm as surfactants. It is worth noting that the excessive amount of OAc is crucial to stabilize the Ag precursor from self-nucleation and avoid the formation of polydisperse AgPd NPs. The morphology of AgPd NPs was investigated using TEM, while the chemical composition of NPs was revealed through ICP-OES. As shown in the TEM images in Fig. 1, the as-synthesized Ag_5Pd_{95}, $Ag_{15}Pd_{85}$, $Ag_{37}Pd_{63}$, and $Ag_{45}Pd_{55}$ NPs are all uniform, with an average size of 4.5 ± 0.3 nm, 3.3 ± 0.4 nm, 2.8 ± 0.5 nm, and 2.3 ± 0.4 nm, respectively. We further prepared 2.4 ± 0.1 nm Ag NPs (Fig. S1a) and 4.8 ± 0.6 nm Pd NPs (Fig. S2a), as described in the experimental section. They are also monodisperse NPs with the similar size as AgPd and can therefore be used in control experiment of electrocatalysis. The use of monodisperse nanoparticles is a key enabler to unambiguously refine the composition effect in catalysis, with the minimized influence from other structural parameters.[27, 28] The as-synthesized NPs were deposited on the Vulcan XC 72R carbon black (C-NPs) and treated with the hydrazine/ethanol solution to remove OAc and OAm bulky hydrophobic surfactants. This process mediated by hydrazine ligand exchange has been widely used for activating the surface of NPs produced with bulky organic ligand for various applications.[29-31] TEM analysis indicates that these NPs well preserved their size, shape and distribution on the carbon support after hydrazine treatment (Fig. S1b, S2b and S3).

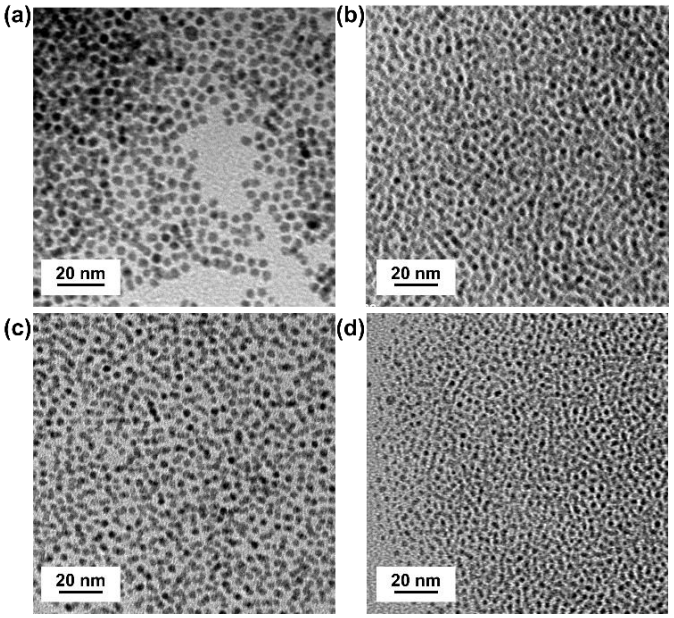

Figure 1.TEM images of as-synthesized (a) Ag_5Pd_{95}, (b) $Ag_{15}Pd_{85}$, (c) $Ag_{37}Pd_{63}$, and (d) $Ag_{45}Pd_{55}$ NPs.

The HRTEM image in Fig. 2a shows that the AgPd NPs remain well crystalline after surfactant removal. Meanwhile, based on STEM high angle annular dark field (HAADF) image and the EELS 2D elemental mappings of AgPd displayed in Fig. 2b-d, we confirmed that Pd and Ag elements are homogeneously distributed in the NPs, forming a solid-solution alloy. The XRD patterns of C-NPs samples were summarized in Fig. S4. It indicates that all NPs present a typical *fcc* structure (Pd: PDF# 03-065-6174; Ag: PDF# 04-0783). The C-Pd displays four diffraction peaks at 40.1°, 45.5°, 68.1°, and 81.3° that are indexed to the (111), (200), (220), and (311) plane diffractions. On C-AgPd and C-Ag samples, only the (111) peak is weakly observed due to the smaller sizes of these NPs, and the peak slightly shifts to the lower angle with the increase of Ag content,

consistent with our previous report.[20] The XPS spectra of AgPd in Fig. S5 displays a negative binding energy (BE) shift of the Pd 3d peak with the decrease in Pd concentration (Table S2). Meanwhile, the Ag 3d peak also shifted negatively. These results agree with the previous theoretical and experimental XPS studies on AgPd alloy materials, evidencing the alloy structure of our AgPd NPs.[32, 33]

The eCO_2RRs on the C-AgPd, C-Pd and C-Ag catalysts were systematically investigated using the CPE technique in the potential range of -0.6 V to -1.0 V vs. RHE. The gas-phase products were simultaneously measured by an on-line GC, while the liquid phase product information was obtained by analysing the catholyte with HPLC after the catalysis. We found that, after two hours of catalysis, both Pd and AgPd NPs structures were well-maintained on the carbon support (Fig. S6, S7a). However, the NPs agglomeration and size increase can be clearly seen on C-Ag after the catalysis testing, which may be caused by the surface redox reactivity of ultrasmall Ag NPs (Fig. S8). Such a redox-induced small NP coalescence during eCO_2RR was also found in the previous studies of Bi,[7] Cu[34] and Pb-based nanocatalysts.[8]

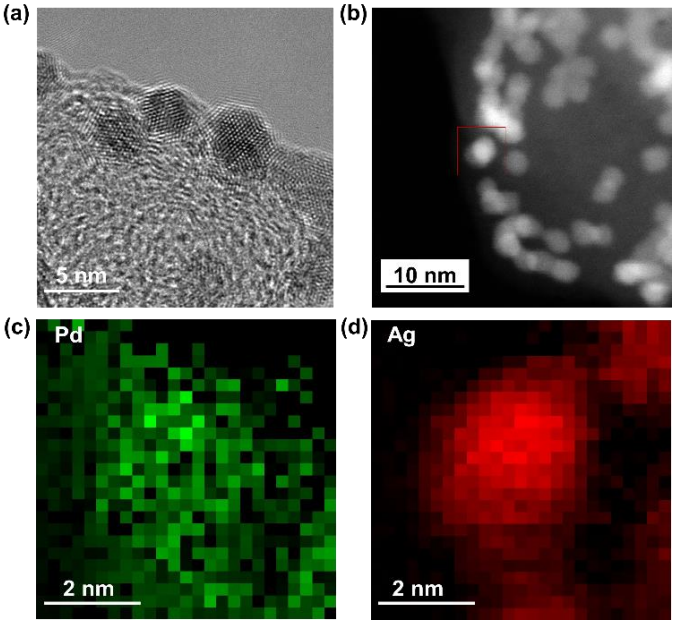

Figure 2. (a) HRTEM image of C-$Ag_{15}Pd_{85}$. (b) HAADF-STEM image and (c, d) corresponding 2D EELS elemental mappings of C-$Ag_{15}Pd_{85}$. The red box in b indicates the area of EELS elemental mappings.

The eCO_2RR catalytic performances of C-AgPd with different bimetallic compositions, along with that of C-Pd and C-Ag, are summarized in Fig. 3. CO is found as the primary product on all catalysts, although the FE_{CO} for each catalyst presents a maximum at different potentials (Fig. 3a). On C-Pd, the maximum FE_{CO} of 83.9 ± 5.9% is obtained at -0.7 V, which is superior to the Pd electrode (<30%)[35] and is comparable to the reported 3.7 nm Pd NPs (91.2%).[14, 36] With lower overpotentials, such as -0.6 V, the FE_{CO} on C-Pd drops down to 42.0 ± 3.8%. At more positive potentials (-0.4 to -0.5 V), liquid-phase formic acid is detected as the primary product without the formation of CO; however, these conditions lead to extremely low current densities (Table S3), suggesting that a certain amount of overpotential is a necessity for *COOH splitting to *CO.[37] The FE_{CO} on C-Pd also decreases at higher overpotentials, due to the limited CO_2 solubility and mass transport and the increased HER rate.[38, 39] Different to Pd, the C-Ag catalyst consistently exhibits a low FE_{CO} (<35%), unless potentials as negative as -0.9 V is applied, which is ascribed to the weak CO adsorption energy on Ag.

The FE_{CO} is substantially improved on C-AgPd NPs catalysts compared with monometallic counterparts, and more interestingly, it presents a volcano-like behaviour in association with bimetallic composition. The C-$Ag_{15}Pd_{85}$ exhibits the highest FE_{CO} across all studied potentials. At -0.8 V and -0.9 V, the FE_{CO} on C-$Ag_{15}Pd_{85}$ reaches 100.0 ± 4.0% and 92.3 ± 2.8% respectively. Even at a low overpotential of -0.6 V, the FE_{CO} still maintains at 88.0 ± 0.5%, which is 1.2 and 3.3 times higher than that of C-Pd and C-Ag, respectively.

We also investigated the eCO_2RR to CO in terms of CO partial current density (j_{CO}), which directly quantifies the CO production rate. As shown in Fig. 3b, all catalysts show an increased CO partial current density at higher overpotentials. The C-Pd also shows a low rate at low overpotentials (~ 0.2 mA cm^{-2} at -0.6 V), which increases to ~ 3.9 mA cm^{-2} at -0.9 V and ~ 4.8 mA cm^{-2} at -1.0 V. The j_{CO} is drastically increased on C-AgPd catalysts. With the best one, C-$Ag_{15}Pd_{85}$, the j_{CO} reaches 3.3 mA cm^{-2} at -0.8 V, leading to an enhancement factor of 1.8 and 8.9 compared with C-Pd and C-Ag.

The current of CO production was further normalized to the total metal mass loading of the catalyst on the electrode to yield mass activity. We found that the bimetallic catalysts clearly enhance the eCO_2RR activity. Especially on C-$Ag_{15}Pd_{85}$, the mass activity reaches 15.2 mA mg^{-1} at -0.8 V, indicating a 2.5- and 3.7-time enhancement compared with C-Pd and C-Ag, respectively.

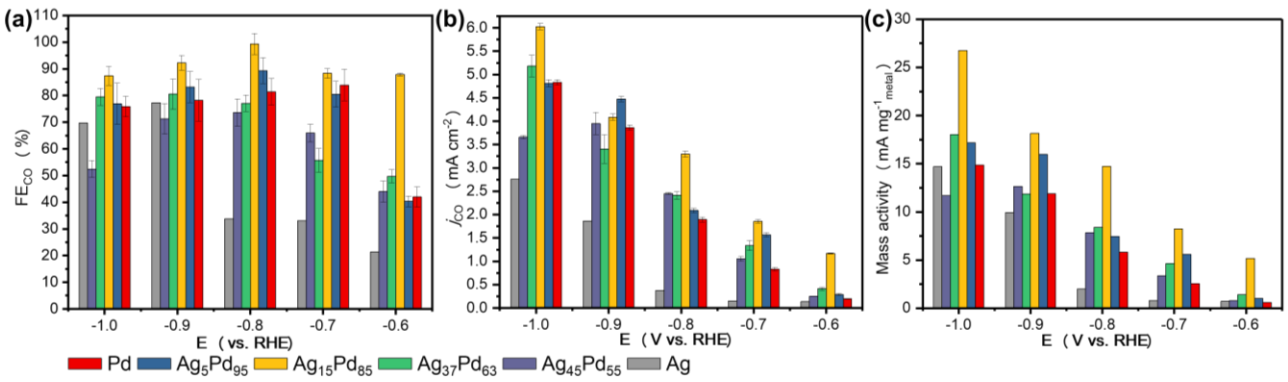

Figure 3. The evaluation of eCO_2 RR performance of C-AgPd, C-Pd, and C-Ag catalysts: (a) Faradic efficiency of CO (FE_{CO}), (b) CO partial current density (j_{CO}); and (c) mass activity at -0.6 to -1.0 V.

C-$Ag_{15}Pd_{85}$ is considered to be the best-performed catalyst for eCO_2RR in all aspects in the present study and exhibits the highest FE_{CO} and mass activity.

The catalytic stability of C-AgPd was evaluated using CPE at -0.8 V for up to 12 hours. As illustrated in Fig. S9, the FE_{CO} on the C-$Ag_{15}Pd_{85}$ is highly stable during the stability testing with the minor fluctuations in the range of 95-100%. After the 12-hour test, the morphology of $Ag_{15}Pd_{85}$ NPs was re-examined under TEM (Fig. S7b). While most of the NP structures are well-preserved, some aggregations are seen in certain areas on the support, and correspondingly, the mass activity is decreased by 12.4 % (from 15.2 mA mg^{-1} to 13.3 mA mg^{-1}) after the 12-hour eCO_2RR (Fig. S9). In comparison, the C-Pd catalyst shows a mass activity decay of 38.6% (from 7.0 mA mg^{-1} to 4.3 mA mg^{-1}) under the same condition (Fig. S10), which is likely resulted from the accumulation of CO over Pd sites,[40] suggesting that bimetallic AgPd NPs catalysts are more durable for long-term eCO_2RR.

As we discussed above, the incorporation of Ag in the AgPd alloy NPs is expected to alleviate the CO-poisoning issue of Pd by weakening the CO adsorption energy in the surface. In principle, such alloy-induced surface energetics change can be possibly rationalized by two effects: ligand and ensemble effects.[41, 42] The ligand effects is described as the change in the chemical properties (chemical state, electronic structure, etc.) of the surface atoms due to alloying. The ensemble effects results from the change in the adsorption and catalytic properties of the surface atom ensembles. Using CO as a probe adsorbate in both experiment and computation, we further studied the surface Pd interaction mode and strength with CO in bimetallic and monometallic catalysts with an objective to understand these two effects.

DRIFTS was used to reveal CO binding configuration and strength with Pd surface atoms, considering that CO is a strong adsorbate with unified interaction with Pd in both gas and solvation conditions. To obtain an optimized IR quality, the AgPd NPs and Pd NPs were loaded onto the alumina (Al_2O_3) instead of carbon black (1 wt% metal loading). The Ag NPs is not included here due to its weak adsorption of CO under ambient conditions. The obtained peak positions and their spectroscopic assignments are listed in Table S4. The stretching frequency of CO on Pd NPs results in several peaks: one peak between 1820 and 1950 cm^{-1} is correlated with multi-centered *CO on threefold hollow and bridge sites, while the linear *CO on atop site usually gives rise to a band at around 2076 cm^{-1}.[43, 44] The former peak is very broad due to the existence of both bridge sites and threefold hollow sites on Pd NPs, which is dominant on Pd catalyst.

A series of IR spectra on three AgPd samples with different compositions were collected under the same conditions (Fig. 4a). It is clearly seen that the relative intensity of different *CO species changes dramatically with the Ag content. The concentration of multi-centered *CO shows a clear-cut and significant drop on $Ag_{15}Pd_{85}$. The drop becomes more intense on the other two samples with the higher Ag content, while the linear *CO dominates in the surface of $Ag_{45}Pd_{55}$ NPs. The multi-centered *CO intensity decrease is ascribed to the dilution effect of Ag, in which Ag, even at low concentration (15%), can effectively disrupt the Pd ensembles in the surface of NPs. In addition, another feature we have noticed is the change in peak positions. As more Pd atoms diluted by Ag are present in the surface, CO coupling between adjacent sites is extenuated, shifting the CO peaks to the lower wavenumber.[45-47,] Such Ag-dilution caused CO peak shifting was also reported in other studies.[46, 48,]

We also investigated the CO binding strength on these NPs by flushing CO-saturated samples with Ar under a series of temperatures and monitor CO-desorption process. The temperature-programmed desorption (TPD) DRIFTS results are shown in Fig. 4b-d and Fig. S11. On both Pd and AgPd NPs, the linear CO_{ad} starts to desorb at a lower temperature, while the energetically more stable multi-centered *CO disappears at a much higher temperature. Based on these, it is clear that the CO adsorbate binds much stronger at the multi-centered Pd sites, while alloying Pd with Ag will result in a disruption of Pd surface ensembles, diminishing the multi-centered *CO adsorption in AgPd NPs surfaces.

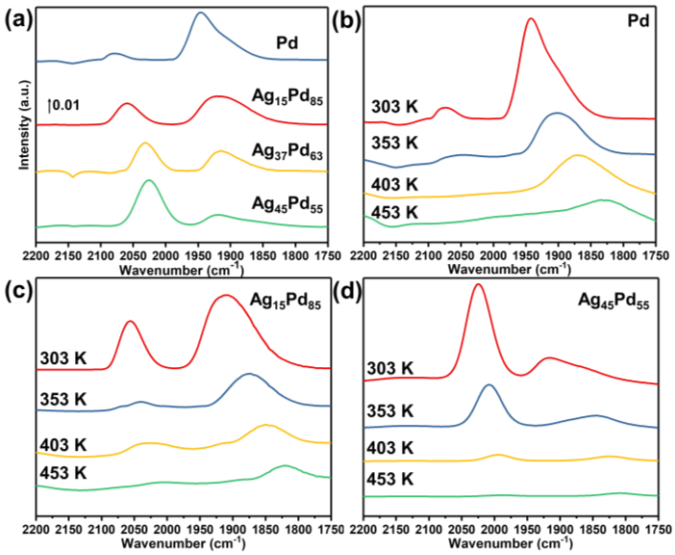

Figure. 4. (a) DRIFTS spectra of alumina-supported Pd, $Ag_{15}Pd_{85}$, $Ag_{37}Pd_{63}$, $Ag_{45}Pd_{55}$ NPs following room temperature CO saturation. (b-d) TPD-DRIFTS spectra of alumina-supported (b) Pd, (c) $Ag_{15}Pd_{85}$ and (d) $Ag_{45}Pd_{55}$ at elevated temperature in an inert atmosphere from 303 K to 453 K following room temperature CO saturation.

DFT calculations were performed to gain a deeper understanding of the impact that Ag-Pd alloying has on CO adsorption strength, an important parameter dictating the CO_2 reduction activity.[10] Ag_xPd_{100-x}(111) surfaces (x = 0, 12.5, 25, 50, 75, and 100) were used for the CO binding energy ($E_{b,CO}$) calculations, as shown in Fig. 5, and Fig. S12. For Ag-rich slab models, surface atoms were rearranged to generate Pd bridge and hollow sites (Fig. 5b-d). As shown for Pd (Fig. 5e), CO was found to most favorably bind in the hollow sites ($E_{b,CO}$ = -1.92 eV at *hcp* site and -1.91 eV at *fcc* site) and least favorably bind on atop sites ($E_{b,CO}$ = -1.38 eV). Upon the introduction of Ag, $E_{b,CO}$ decreases for each Pd binding site. Due to the weak CO binding nature of Ag, mixed AgPd sites are less important, as $E_{b,CO}$ at these sites are generally lower than those of the adjacent Pd only sites (Fig. S13).

The initial weakening of $E_{b,CO}$ conflicts with the calculated d-band centers that rise with addition of Ag up to 50% (Fig. S14). A contradiction is also seen by comparing $E_{b,CO}$ from the AgPd alloys to that of strained Pd (Fig. S15). The tensile strain introduced by Ag would ordinarily strengthen $E_{b,CO}$; however, that is clearly not the case we observed in AgPd NPs. This has previously been discussed by Abild-Pedersen et al.[49] and is due to an asymmetry in the Pd d-band formed from an energy misalignment with the Ag d orbitals. They adopt an alternative descriptor, ε_u, defined as the highest peak position of the surface atom d-band Hilbert transform. This

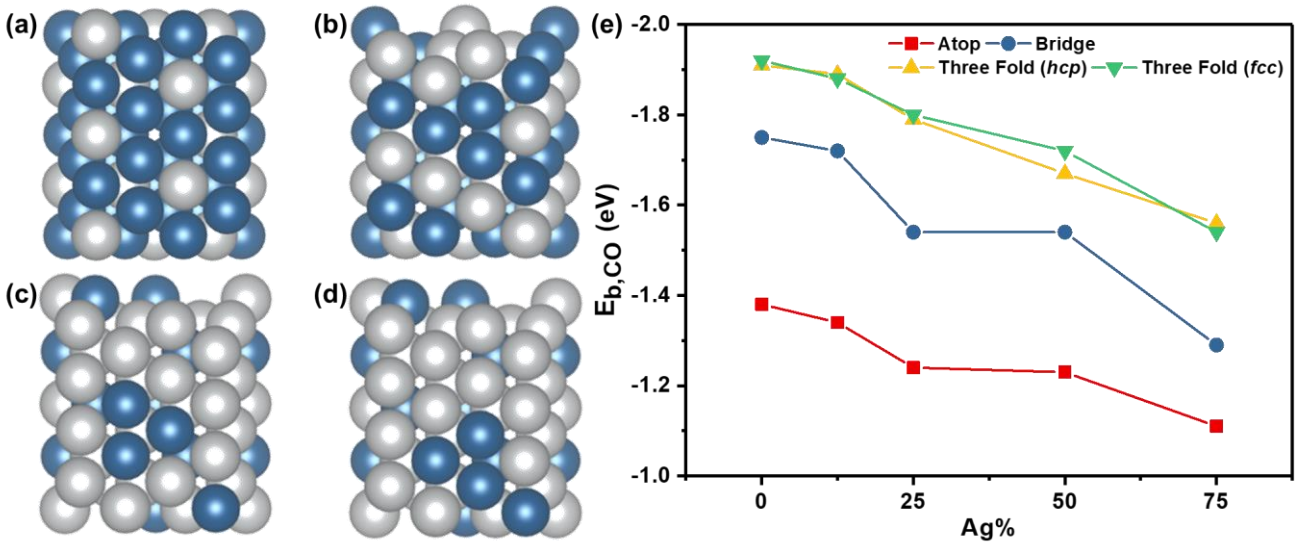

Figure 5. Calculated surface slabs of (a) $Ag_{25}Pd_{75}$(111), (b) $Ag_{50}Pd_{50}$(111) with surface atoms rearranged to generate bridge and three-fold hollow Pd sites, (c, d) $Ag_{75}Pd_{25}$ (111) with (c) bridge and hcp Pd three-fold hollow sites, and (d) with bridge and fcc Pd three-fold hollow sites. The silver atoms represent Ag and blue atoms represent Pd. (e) CO adsorption energies $E_{b,CO}$ at the different Pd sites calculated for AgPd alloys of varying Ag concentrations (Ag%). In general, the binding energy decreases with increasing Ag concentration and with fewer participating Pd atoms.

descriptor better correlates to the antibonding orbital of the absorbate as described in the Newns-Anderson binding model.[50-52] In performing this analysis for our calculations, we find excellent agreement (Fig. S14, S16-S18). Up to 50% doping, ε_u decreases by 0.4 eV and binding energies average a 0.18 eV reduction. Between 50% and 75% doping, however, there is a much greater decrease in ε_u of 0.75 eV and the binding energies are reduced another 0.17 eV.

The weakening of $E_{b,CO}$ is important to improving the CO_2 reduction activity since Pd ordinarily binds CO too strongly. We can summarize these calculations by describing two ways in which Ag reduces $E_{b,CO}$. First, there is a strong ligand effect that is introduced by Ag. This results in a large perturbation to the Pd d-band shape. The second means, the ensemble effect, is by reducing the number of multi-centered Pd adsorption sites on the surface. Relative to the ligand effect, the ensemble effect generates much greater reductions in $E_{b,CO}$ at lower Ag concentrations. This is critical because Ag is not important for the activation of CO_2 until high overpotentials, and only Pd sites matter. This ensemble effect is the primary source of the observed volcano relationship. Just enough Ag (15%) is needed to break up multi-centered hollow sites, providing balanced surface energetics for CO_2 activation as well as CO desorption. Further addition of Ag reverses this balance and lowers overall activity due to the barrier of CO_2 activation.

Conclusions

In summary, we synthesized monodisperse AgPd alloy NPs with tunable bimetallic compositions and investigated their catalytic properties for eCO_2 RR. It was found that the catalytic performance for the CO production was enhanced and controlled by the bimetallic composition of NPs, with the $Ag_{15}Pd_{85}$ demonstrating the best performance with high activity, selectivity, and durability at low overpotentials. At -0.8 V, $Ag_{15}Pd_{85}$reached a FE_{CO} of 100% with a mass activity of 15.2 mA mg_{metal}^{-1}. The DFT calculations and DRIFTS measurements elucidated that alloying with Ag alleviated the over-strong adsorption of CO over Pd, accelerating eCO_2 RR to CO kinetics. This modulation was found to be caused by two effects, i.e., Ag weakens the CO adsorption at all possible Pd sites via the ligand effect and diminishes the strongest CO-binding sites, multi-centered hollow sites in favor of weaker binding atop sites via the ensemble effect.

Conflicts of Interest

There are no conflicts of interest to declare.

Acknowledgment

This work was supported by 4-VA Collaborative Research Grant Program. This research used resources of the Center for Functional Nanomaterials, which is a U.S. DOE Office of Science Facility, at Brookhaven National Laboratory under Contract No. DE-SC0012704. This research used the PHI Versaprobe III XPS within the Nanoscale Materials Characterization Facility (NMCF) in the University of Virginia; we acknowledge NSF MRI Award 1626201 for the acquisition of this instrument.

References

1. D. T. Whipple and P. J. A. Kenis, *J. Phys. Chem. Lett.*, 2010, **1**, 3451-3458.
2. G. Centi and S. Perathoner, *Catal. Today*, 2009, **148**, 191-205.
3. M. Aresta, A. Dibenedetto and A. Angelini, *Chem. Rev.*, 2014, **114**, 1709-1742.
4. M. G. Kibria, J. P. Edwards, C. M. Gabardo, C.-T. Dinh, A. Seifitokaldani, D. Sinton and E. H. Sargent, *Adv. Mater.*, 2019, **31**, 1807166.
5. J. Schneider, H. Jia, J. T. Muckerman and E. Fujita, *Chem. Soc. Rev.*, 2012, **41**, 2036-2051.

6. R. P. S. Chaplin and A. A. Wragg, *J. Appl. Electrochem.*, 2003, **33**, 1107-1123.
7. Z. Zhang, M. Chi, G. M. Veith, P. Zhang, D. A. Lutterman, J. Rosenthal, S. H. Overbury, S. Dai and H. Zhu, *ACS Catal.*, 2016, **6**, 6255-6264.
8. Z. Zhang, C. Liu, J. T. Brosnahan, H. Zhou, W. Xu and S. Zhang, *J. Mater. Chem. A*, 2019, **7**, 23775-23780.
9. W. Zhu, S. Kattel, F. Jiao, J., Chen, *Adv. Energy Mater.*, 2019, **9**, 1802840.
10. A. A. Peterson and J. K. Norskov, *J. Phys. Chem. Lett.*, 2012, **3**, 251-258.
11. Y. Peng, M. Cui, Z. Zhang, S. Shu, X. Shi, J. T. Brosnahan, C. Liu, Y. Zhang, P. Godbold, X. Zhang, F. Dong, G. Jiang and S. Zhang, *ACS Catal.*, 2019, **9**, 10803-10811.
12. P. Albers, J. Pietsch, S. F., Parker, *J. Mol. Catal. A Chem.*, 2001, **173**, 275-286.
13. D. Gao, H. Zhou, F. Cai, J. Wang, G. Wang and X. Bao, *ACS Catal.*, 2018, **8**, 1510-1519.
14. D. Gao, H. Zhou, J. Wang, S. Miao, F. Yang, G. Wang, J. Wang and X. Bao, *J. Am. Chem. Soc.*, 2015, **137**, 4288-4291.
15. H. Dong, L. Zhang, P. Yang, X. Chang, W. Zhu, X. Ren, Z. Zhao and J. Gong, *Chem. Eng. Sci.*, 2019, **194**, 29-35.
16. Z. Yin, D. Gao, S. Yao, B. Zhao, F. Cai, L. Lin, P. Tang, P. Zhai, G. Wang, D. Ma and X. Bao, *Nano Energy*, 2016, **27**, 35-43.
17. J. H. Lee, S. Kattel, Z. Jiang, Z. Xie, S. Yao, B. M. Tackett, W. Xu, N. S. Marinkovic and J. G. Chen, *Nat. Commun.*, 2019, **10**, 3724.
18. X. Bai, W. Chen, C. Zhao, S. Li, Y. Song, R. Ge, W. Wei and Y. Sun, *Angew. Chem. Int. Ed.*, 2017, **56**, 12219-12223.
19. Y. Wang, L. Cao, N. J. Libretto, X. Li, C. Li, Y. Wan, C. He, J. Lee, J. Gregg, H. Zong, D. Su, J. T. Miller, T. Mueller and C. Wang, *J. Am. Chem. Soc.*, 2019, **141**, 16635-16642.
20. S. Zhang, O. Metin, D. Su and S. Sun, *Angew. Chem. Int. Ed.*, 2013, **52**, 3681-3684.
21. V. Mazumder and S. Sun, *J. Am. Chem. Soc.*, 2009, **131**, 4588-4589.
22. G. Kresse and D. Joubert, *Phys. Rev. B*, 1999, **59**, 1758-1775.
23. P. E. Blöchl, *Phys. Rev. B* , 1994, **50**, 17953-17979.
24. B. Hammer, L. B. Hansen and J. K. Nørskov, *Phys. Rev. B*, 1999, **59**, 7413-7421.
25. H. J. Monkhorst and J. D. Pack, *Phys. Rev. B*, 1976, **13**, 5188-5192.
26. O. M. Løvvik and R. A. Olsen, *J. Alloys Compd.*, 2002, **330-332**, 332-337.
27. Z. Zhang, Q. Wu, G. Johnson, Y. Ye, X. Li, N. Li, M. Cui, J. D. Lee, S. Zhao, S. Li, A. Orlov, C. B. Murray, X. Zhang, T. B. Gunnoe, D. Su, S. Zhang, *J. Am. Chem. Soc.,* 2019, **141**, 16548-16552
28. Y. Zhang, N. Li, Z. Zhang, S. Li, M. Cui, L. Ma, H. Zhou, D. Su, S. Zhang, *J. Am. Chem. Soc.,* 2020, doi.org/10.1021/jacs.0c02584
29. D. V. Talapin and C. B. Murray, *Science*, 2005, **310**, 86.
30. G. Zhang, B. Kirk, L. A. Jauregui, H. Yang, X. Xu, Y. Chen and Y. Wu, *Nano Lett.*, 2012, **12**, 56-60.
31. M. Law, J. M. Luther, Q. Song, B. K. Hughes, C. L. Perkins and A. J. Nozik, *J. Am. Chem. Soc.*, 2008, **130**, 5974-5985.
32. I. A. Abrikosov, W. Olovsson and B. Johansson, *Phys. Rev. Lett.*, 2001, **87**, 176403.
33. W. Olovsson, C. Göransson, L. Pourovskii, B. Johansson and I. A. Abrikosov, *Phys. Rev. B*, 2005, **72**, 064203.
34. O. Baturina, Q. Lu, F. Xu, A. Purdy, B. Dyatkin, X. Sang, R. Unocic, T. Brintlinger and Y. Gogotsi, *Catal. Today*, 2017, **288**, 2-10.
35. Y. Hori, H. Wakebe, T. Tsukamoto and O. Koga, *Electrochim. Acta*, 1994, **39**, 1833-1839.
36. F. Cai, D. Gao, H. Zhou, G. Wang, T. He, H. Gong, S. Miao, F. Yang, J. Wang and X. Bao, *Chem. Sci.*, 2017, **8**, 2569-2573.
37. R. Kortlever, I. Peters, S. Koper and M. T. M. Koper, *ACS Catal.*, 2015, **5**, 3916-3923.
38. H. Ooka, M. C. Figueiredo and M. T. M. Koper, *Langmuir*, 2017, **33**, 9307-9313.
39. D. Ren, J. Fong and B.S. Yeo, *Nat. Commun.*, 2018, **9**, 925.
40. D. Gao, H. Zhou, F. Cai, D. Wang, Y. Hu, B. Jiang, W. Cai, X. Chen, R. Si, F. Yang, S. Miao, J.Wang, G. Wang and X. Bao, *Nano Res.*, 2017, **10**, 2181-2191.
41. M. Chen, D. Kumar, C. Yi and D. W. Goodman, *Science*, 2005, **310**, 291-293.
42. P. Liu and J. K. Nørskov, *Phys. Chem. Chem. Phys.*, 2001, **3**, 3814-3818.
43. K. Wolter, O. Seiferth, H. Kuhlenbeck, M. Baumer and H. J. Freund, *Surf. Sci.*, 1998, **399**, 190-198.
44. S. Bertarione, D. Scarano, A. Zecchina, V. Johánek, J. Hoffmann, S. Schauermann, M. M. Frank, J. Libuda, G. Rupprechter and H.-J. Freund, *J. Phys. Chem. B*, 2004, **108**, 3603-3613.
45. J. Mink, G. Keresztury, T. Szilágyi and P. Tétényi, *J. Mol. Struct*., 1993, **293**, 283-286.
46. Y. Han, J. Sun, H. Fu, X. Qu, H. Wan, Z. Xu and S. Zheng, *Appl. Catal. A: Gen.*, 2016, **519**, 1-6.
47. Y. Ma, T. Diemant, J. Bansmann and R. J. Behm, *Phys. Chem. Chem. Phys.*, 2011, **13**, 10741-10754.
48. M. R. Ball, K. R. Rivera-Dones, E. Stangland, M. Mavrikakis and J. A. Dumesic, *J. Catal.*, 2019, **370**, 241-250.
49. H. Xin, A. Vojvodic, J. Voss, J. K. Norskov and F. Abild-Pedersen, *Phys. Rev. B*, 2014, **89**.
50. P. W. Anderson, *Phys. Rev.*, 1961, **124**, 41-53.
51. D. M. Newns, *Phys. Rev.*, 1969, **178**, 1123-1135.
52. J. P. Muscat and D. M. Newns, *Prog. Surf. Sci.*, 1978, **9**, 1-43.

Table of contents:

By balancing bimetallic composition-associated ligand and ensemble effects, $Ag_{15}Pd_{85}$ nanoparticles show an enhanced catalytic property for electrochemical CO_2 reduction.